



Published in final edited form as:

J Mater Chem B. 2021 May 14; 9(18): 3826–3837. doi:10.1039/d0tb02987d.

Shape memory polymer (SMP) scaffolds with improved self-fitting properties

Michaela R. Pfau^a, Kelly G. McKinzey^a, Abigail A. Roth^a, Lance M. Graul^a, Duncan J. Maitland^a, Melissa A. Grunlan^{*,a,b,c}

^aDepartment of Biomedical Engineering, Texas A&M University, College Station, TX 77843, USA.

^bDepartment of Materials Science and Engineering, Texas A&M University, College Station, TX 77843, USA.

^cDepartment of Chemistry, Texas A&M University, College Station, TX 77843, USA.

Abstract

“Self-fitting” shape memory polymer (SMP) scaffolds prepared as semi-interpenetrating networks (semi-IPNs) with crosslinked *linear*-poly(*ε*-caprolactone)-diacrylate (PCL-DA, $M_n \sim 10$ kg/mol) and *linear*-poly(L-lactic acid) (PLLA, $M_n \sim 15$ kg/mol) [75/25 wt%] exhibited robust mechanical properties and accelerated degradation rates versus a PCL-DA scaffold control. However, their potential to treat irregular craniomaxillofacial (CMF) bone defects is limited by their relatively high fitting temperature ($T_{fit} \sim 55$ °C; related to the T_m of PCL) required for shape recovery (i.e. expansion) and subsequent shape fixation during press fitting of the scaffold, which can be harmful to surrounding tissue. Additionally, the viscosity of the solvent-based precursor solutions, cast over a fused salt template during fabrication, can limit scaffold size. Thus, in this work, analogous semi-IPN SMP scaffolds were also formed with a 4-arm *star*-PCL-tetracrylate (*star*-PCL-TA) ($M_n \sim 10$ kg/mol) and *star*-PLLA ($M_n \sim 15$ kg/mol). To assess the impact of a *star*-polymer architecture, four semi-IPN compositions were prepared: *linear*-PCL-DA/*linear*-PLLA (*L/L*), *linear*-PCL-DA/*star*-PLLA (*L/S*), *star*-PCL-TA/*linear*-PLLA (*S/L*) and *star*-PCL-TA/*star*-PLLA (*S/S*). Two PCL controls were also prepared: *LPCL* (i.e. 100% *linear*-PCL-DA) and *SPCL* (i.e. 100% *star*-PCL-TA). The *S/S* semi-IPN scaffold exhibited particularly desirable properties. In addition to achieving a lower, tissue-safe T_{fit} (~ 45 °C), it exhibited the fastest rate of degradation which is anticipated to more favourably permit neotissue infiltration. The radial expansion pressure exerted by the *S/S* semi-IPN scaffold at T_{fit} was greater than that of *LPCL*, which is expected to enhance osseointegration and mechanical stability. The intrinsic viscosity of the *S/S* semi-IPN macromer solution was also reduced such that larger scaffold specimens could be prepared.

Graphical Abstract

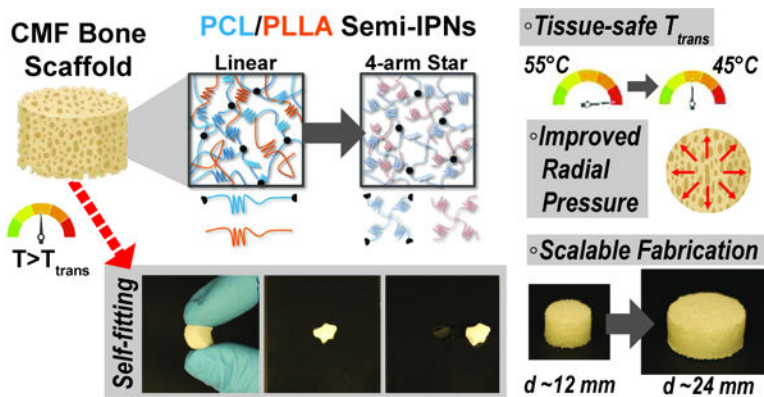
*Corresponding Author, mgrunlan@tamu.edu, Tel: +1 979 845 2406.

Author Contributions

The manuscript was written through contributions of all authors. All authors have given approval to the final version of the manuscript.

Conflicts of interest

There are no conflicts to declare.



Introduction

A major limitation of biologic and alloplastic grafts used to treat irregularly shaped cranio-maxillofacial (CMF) bone defects is the difficulty in achieving sufficient bone-to-graft contact, essential for osseointegration and healing.^{1, 2} Autografting remains the clinical “gold standard”, but in addition to the demands of surgical harvesting, bone graft rigidity contributes to poor shaping and tissue contact, ultimately leading to graft resorption.^{3–5} Synthetic CMF bone graft substitutes, including ceramic injectables⁶ and bone cements,⁷ utilize *in situ* curing to achieve a defect-specific fit. However, they are limited by risks associated with brittle mechanical properties (leading to post-surgical fracture), exothermic curing (leading to tissue damage), and shrinkage post-cure (leading to poor bone-to-graft contact).^{8–10} PEEK implants can be formed with patient-specific geometry via 3D printing, but are non-regenerative.^{7, 11} Thus, an off-the-shelf regenerative scaffold material that can readily achieve conformal fit into irregular CMF bone defects is expected to improve healing outcomes.

We have previously reported “self-fitting” scaffolds based on thermoresponsive shape memory polymers (SMPs) as a regenerative approach to treat CMF bone defects.^{12–16} Porous SMP scaffolds were prepared from *linear*-poly(ϵ -caprolactone) diacrylate (*linear*-PCL-DA, $M_n \sim 10$ kg/mol) by photocuring a solvent-based macromer solution over a fused salt template followed by aqueous extraction of the template (i.e. solvent-casting/particulate leaching, SCPL). For such PCL SMP scaffolds, covalent cross-links act as netpoints and PCL lamellae act as switching segments. In a surgical setting, the PCL scaffolds could be warmed in saline to their “fitting temperature” ($T_{fit} \sim 55$ °C, related to $T_{m,PCL}$), causing the PCL lamellae to begin to melt and the scaffold to subsequently soften. It could thus be readily press-fitted into the defect site as shape recovery would drive expansion of the scaffold to the perimeter. Then, as the scaffold would cool to body temperature ($T < T_{fit}$), the PCL lamellae would re-crystallize and return the scaffold to its relatively rigid state with the scaffold fixed into the shape of the defect. Importantly, the PCL SMP scaffolds displayed high shape fixity and recovery, non-brittle mechanical properties, and high pore interconnectivity.^{12–15} Increasing the rigidity of the PCL scaffolds would improve structural support in the early stages of healing and increasing the rate of degradation would promote osseointegration and regeneration.^{17–21} Thus, thermoplastic *linear*-poly(L-lactic acid)

(PLLA, ~15 kg/mol) was incorporated into thermoset *linear*-PCL-DA networks to yield *linear*-PCL-DA/*linear*-PLLA semi-interpenetrating network (semi-IPN) scaffolds.^{16, 22} A semi-IPN scaffold prepared with 75/25 wt% PCL/PLLA maintained SMP behavior ($T_{fit} \sim 55$ °C), but demonstrated an increased modulus and accelerated degradation rate compared to the *linear*-PCL-DA control. The faster degradation of the *linear*-PCL-DA/*linear*-PLLA semi-IPNs was linked to polymer phase separation.^{16, 23, 24} Likewise, phase separation has been shown to impact mechanical and degradation properties of polyester blends.^{25–28}

Further improvements to mechanical and degradation properties of PCL-based SMP scaffolds, as well as reducing the T_{fit} (to avoid possible tissue damage) and reducing macromer solution viscosity (to aid in scaffold fabrication), would be a significant enhancement in their utility. Because of their unique thermal, degradative, mechanical, and rheological properties,^{29–31} *star*-polymer analogues may offer distinct advantages to the PCL/PLLA semi-IPN scaffolds. T_m values of multi-arm polymers are typically reduced due in part to their more sterically hindered architectures.^{32–34} Biodegradable *star* polyesters have also been employed to refine degradation behavior.^{32, 35, 36} Additionally, *star*-polymers are associated with reduced hydrodynamic volumes which affects dispersion and interfacial macromolecular interactions.^{37, 38} Thus, *star*-polymers have been used to improve miscibility and resulting toughness of blends and polymer nanocomposites.^{39–42} Lastly, *star*-polymers are well known for having reduced dilute solution viscosities due to less chain entanglements relative to their linear counterparts.^{43, 44} In the fabrication of SMP scaffolds, during solvent casting of the macromer solution over a fused salt template, this could aid in diffusion such that larger scaffold specimens could be readily prepared.

Herein, towards favorable tuning of semi-IPN scaffold properties, the impact of a crosslinkable 4-arm *star*-PCL analogue and thermoplastic 4-arm *star*-PLLA was assessed. Specifically, scaffold compositions were systematically made with combinations of *linear*-PCL-DA or *star*-PCL-tetracrylate (*star*-PCL-TA) and *linear*-PLLA or *star*-PLLA: *linear*-PCL-DA/*linear*-PLLA (*L/L*), *linear*-PCL-DA/*star*-PLLA (*L/S*), *star*-PCL-TA/*linear*-PLLA (*S/L*) and *star*-PCL-TA/*star*-PLLA (Figure 1a). The ratio of PCL/PLLA was maintained at 75/25 wt%, that of the *L/L* semi-IPN previously shown to best enhance compressive modulus and degradation rate versus the *linear*-PCL-DA control (*LPCL*) (i.e. 100% PCL-DA).^{16, 22} In addition to the *LPCL* control, a *star*-PCL-TA control (*SPCL*) (i.e. 100% PCL-TA) was also prepared. All scaffolds were prepared with the same SCPL protocol to generate scaffolds with similar pore size and interconnectivity (Figure 1b). The resulting SMP scaffolds were assessed for their thermal, degradative, mechanical, and shape memory properties. The solution viscosity of macromer solutions used in the SCPL fabrication process was also examined and select compositions were used to fabricate scaffolds with larger dimensions.

Experimental

Materials

Linear-PCL-diol ($M_n = 10$ kg/mol per manufacturer specifications), 4-(dimethylamino)pyridine (DMAP), triethylamine (Et_3N), acryloyl chloride, potassium carbonate (K_2CO_3), anhydrous magnesium sulfate ($MgSO_4$), sodium chloride (NaCl, salt),

(3*S*)-*cis*-3,6-dimethyl-1,4-dioxane-2,5-dione (L-lactide), ϵ -caprolactone, pentaerythritol, tin(II) 2-ethylhexanoate (Sn(Oct)₂), ethylene glycol, 2,2-dimethoxy-2-phenyl acetophenone (DMP), 1-vinyl-2-pyrrolidinone (NVP), sodium hydroxide (NaOH), deuterated chloroform (CDCl₃), and solvents were purchased from Sigma-Aldrich. All solvents and ethylene glycol were dried over 4 Å molecular sieves, all reagents were vacuum dried overnight (ON), and all glassware and stir bars were dried at 120 °C ON prior to use. Salt was sieved using an ASTM E-11 no.40 and no. 35 sieves with 425 μm and 500 μm openings respectively; scanning electron microscopy (SEM) and ImageJ showed an average salt size of 460 ± 70 μm.

Methods

Syntheses—All reactions were run under a nitrogen (N₂) atmosphere with a Teflon-covered stir bar. Following purification, polymer structures (including % acrylation, architecture, and M_n) were confirmed with ¹H NMR spectroscopy (Inova 500 MHz spectrometer in FT-mode with CDCl₃ as the standard). Polymer thermal properties were determined using differential scanning calorimetry (DSC, TA Instruments Q100) as described below.

Thermoplastic *linear*- and *star*-PLLA (M_n ~15 kg/mol) were synthesized via ring opening polymerizations (ROPs) according to an established protocol.⁴⁵ L-lactide (6.0 g), alcohol initiator, and Sn(Oct)₂ catalyst were allowed to react ON at 120 °C. The alcohol initiator was varied from difunctional ethylene glycol to tetrafunctional pentaerythritol to achieve a *linear*- and *star*-PLLA architecture, respectively. M_n was controlled via molar equivalence of monomer to initiator (104:1, [M]:[I]). The crude products were dissolved in a minimal amount of chloroform and were precipitated into methanol. Final products were filtered and vacuum dried (RT, ON, 30 in. Hg) to obtain purified *linear*- and *star*-PLLA. Target M_n and architecture were verified using ¹H NMR end group analysis (CH δ = 5.2 ppm in repeat unit compared to terminal CH δ = 3.7 ppm). The following thermal transitions were observed for *linear*-PLLA [T_g = 45 °C, T_m = 155 °C, 50% crystallinity] and *star*-PLLA [T_g = 49 °C, T_m = 152 °C, 15% crystallinity] (Figure S1).

Star-PCL-tetrol was synthesized via ROP (analogous to that described above) with a target M_n of ~10 kg/mol to match that of *linear*-PCL-diol (M_n = 10 kg/mol; Sigma-Aldrich). The ϵ -caprolactone (25.0 g), pentaerythritol (88:1, [M]:[I]) and Sn(Oct)₂ were combined and were allowed to react ON at 120 °C. The crude product was re-dissolved and precipitated as described above to yield purified *star*-PCL-tetrol. The target M_n and architecture were verified via ¹H NMR end group analysis (CH₂ δ = 4.1 ppm in repeat unit compared to terminal CH₂ δ = 3.7 ppm). Thermal transitions were determined for both the *linear*-PCL-diol [T_g = -65 °C, T_m = 53 °C, 48% crystallinity] and the *star*-PCL-tetrol [T_g = -63 °C, T_m = 50 °C, 45% crystallinity] (Figure S2).

Linear-PCL-diol and *star*-PCL-tetrol were acrylated to form photo-crosslinkable *linear*-PCL-DA and *star*-PCL-TA macromers, respectively, using established acrylation protocols.¹⁵ Briefly, *linear*-PCL-diol (20.0 g, 2.0 mmol) was combined with DMAP (6.6 mg) serving as the catalyst and they were dissolved in dichloromethane (DCM, 0.17 g/mL). After purging with N₂, triethylamine (4.0 mmol) and acryloyl chloride (8.0 mmol) were added to the flask

and the reaction was left to stir at RT for 30 min. An analogous procedure was followed for the *star*-PCL-tetrol but molar ratios were doubled to account for the 4 end groups [DMAP = 13.2 mg, triethylamine = 8.0 mmol, acryloyl chloride = 16.0 mmol]. Established work-up procedures were followed to obtain *linear*-PCL-DA and *star*-PCL-TA.¹⁵ Percent acrylation was confirmed via ¹H NMR end group analysis (CH_2 δ = 4.1 ppm in repeat unit, compared to acrylate protons $\text{CH}=\text{CH}_2$ δ = 5.6, 6.1 and 6.4 ppm) to be > 85% for both *linear*-PCL-DA and *star*-PCL-TA (Figure S3).

Fabrication

Scaffolds.: Porous scaffolds were prepared via SCPL, based on a previous report,¹⁵ employing a fused salt template for pore interconnectivity. Sieved NaCl (10.0 g, 460 ± 70 μm) was placed in a 20 mL scintillation vial (I.D. = 25 mm) and DI water (7.5 wt%) was added in four portions followed by manual stirring with a spatula after each addition. The wet salt was pressed with a glass rod and the vials were centrifuged (15 min, 3220 x g). The opened vials were air dried for ~ 1 hr and were subsequently vacuum dried (RT, ON, 30 in. Hg).

Next, macromer solutions were prepared by dissolving a designated macromer or combination of two macromers (75/25 wt% ratio) in DCM (0.15 g total per mL DCM). Photoinitiator solution (10 wt % DMP in NVP) was then added at 15 vol%. To each salt template ~5 mL of macromer solution was added and the vials were centrifuged (10 min, 1260 x g) to promote macromer solution diffusion throughout the template. To crosslink acrylated macromers, opened vials were then exposed to UV light for 5 min (UV-Transilluminator, 6 mW cm^{-2} , 365 nm) followed by air drying in a fume hood ON. To remove the salt template, vials were then placed in a solution of water and ethanol (1:1 by vol.) for ~5 days with daily solution changes. Resulting porous scaffolds were air dried ON, and finally heat treated (170 °C, 10 min, 30 in. Hg). The dried scaffolds (d ~12 mm) were sliced into three specimens (t ~2 mm) (Vibratome, Leica VT 1000 S) and were biopsy punched (Integra Miltex, 6 mm). Final specimen dimensions were d ~6 mm x t ~ 2mm.

Solid Films.: Analogous solid films of each scaffold composition were prepared for % porosity calculations and to evaluate polymer miscibility in film cross-sections. A macromer solution (25 wt% total polymer in DCM), combined with the aforementioned photoinitiator solution (15 vol%), was added to a circular silicone mold (d ~45 mm x t ~2 mm; McMaster-Carr) secured between 2 glass slides. The mold was then exposed to UV-light (UV Transilluminator, 6 mW cm^{-2} , 365 nm) for 3 min on each side. The swollen films were air dried ON followed by vacuum drying (RT, 4 hr, 30 in. Hg), soaking in ethanol while placed atop a shaker table (150 rpm, 3 hr), air drying ON, and finally, heat treated (170 °C, 30 min, 30 in. Hg). Films were punched to form disc specimens (d ~5 mm x t ~1.1 mm) used for testing.

Scaffold Sol Content—Scaffolds (d ~6 mm x t ~2 mm; $N=3$) were each submerged in 10 mL of DCM in a scintillation vial. Sealed vials were placed atop a shaker table (150 rpm, 48 hr) and scaffolds were subsequently rinsed with DCM, air dried, and dried under vacuum (RT, ON, 30 in. Hg). Initial and final mass values were used to calculate % sol content.

Thermal gravimetric analysis (TGA)—TGA (TA Instruments Q50) of scaffolds (~10 mg; $N = 1$) was performed under N_2 from RT to 500 °C (heating rate = 10 °C/min) using platinum pans.

% Porosity—The percent porosity of scaffolds ($N = 3$) was determined gravimetrically using Equation 1:

$$\text{Porosity}(\%) = \frac{\rho_{\text{solid film}} - \rho_{\text{porous scaffold}}}{\rho_{\text{solid film}}} * 100 \quad (1)$$

where $\rho_{\text{porous scaffold}}$ is the density of the final scaffold specimens and $\rho_{\text{solid films}}$ is the density of analogous solid film samples.

Pore size—Scaffold pore interconnectivity and pore size were evaluated with SEM (JEOL JCM-5000 Neoscope, accelerating voltage ~10 kV) following coating with Au-Pt (~4 nm). Scaffold images ($n = 4$) were analyzed using image analysis software (Image J); measurements ($N = 30$) were taken from pores along the diagonal midline to determine average pore size.

Thermal transitions and % crystallinity—Differential scanning calorimetry (DSC; TA Instruments Q100) was used to determine T_g , T_m , and % crystallinity of PCL and PLLA polymers prior to scaffold fabrication. Specimens (~10 mg; $N = 3$) were sealed in hermetic pans and heated at a rate of 10 °C/min, and values were taken from the second cycle to erase thermal history. The onset and midpoint of $T_{m,PCL}$ and $T_{m,PLLA}$ was determined using TA Universal Analysis software from the onset and the maximum of the endothermic melt peak, respectively. Percent crystallinity was determined with Equation 2:

$$\% \chi_c = \frac{\Delta H_m - \Delta H_c}{\Delta H_m^\circ} * 100 \quad (2)$$

where ΔH_m is the enthalpy of fusion taken from the integral of the endothermic melt peak, ΔH_c is the enthalpy of crystallization from the exothermic cold crystallization peak and ΔH_m° is the theoretical value for 100% crystalline PCL (139.5 J/g)⁴⁶ or PLLA (93.0 J/g).⁴⁷

Scaffolds ($N = 3$) were likewise examined but using a heating rate of 5 °C/min and using the first cycle to examine the impact of fabrication. For semi-IPNs (PCL/PLLA 75/25 wt%), a correction factor to account for polymer wt% was included in % crystallinity calculations according to Equation 3:

$$\% \chi_c = \frac{\Delta H_m - \Delta H_c}{\Delta H_m^\circ * w} * 100 \quad (3)$$

where w is the mass fraction of the designated polymer species (i.e. $w = 0.75$ for PCL and $w = 0.25$ for PLLA in semi-IPN compositions).

Degradation—Degradation tests were performed under base-catalyzed conditions (0.2 M NaOH) according to ASTM F1635. Scaffold specimens (d ~6 mm x t ~2mm; $N=3$ per time point) were each submerged in 10 mL of the basic solution in a sealed glass vial and maintained in an incubator (VWR Benchtop Shaking Incubator Model 1570) at 37 °C and 60 rpm. At each of the five designated time points (24, 48, 72, 120, and 168 h), samples were removed, thoroughly rinsed with DI water, blotted, and finally dried under vacuum (RT, ON, 30 in. Hg). Specimen mass was measured to examine gravimetric mass loss.

Compressive mechanical properties—Scaffold specimens (d ~6 mm x t ~2 mm; $N=3$) underwent static compression testing (Instron 5944) at RT. Specimens were subjected to a constant strain (1.5 mm/min) up to 85% strain. Due to their non-brittle nature, no specimen fractured. The average compressive modulus (E), strength (CS), and toughness were reported: E was determined from the initial linear region ($< 10\% \epsilon$). CS was determined from the stress at 85% strain. Toughness values were calculated from the area of the stress-strain curves up to 85% strain.

Shape memory properties

Self-fitting behavior in model defect.: Scaffold specimens (d ~6 mm x t ~2 mm; $N=3$) were evaluated for their “self-fitting” ability using a model defect representative a rat calvarial defect.^{48, 49} From an ultra-high-molecular-weight polyethylene (UHMWPE) sheet (McMaster-Carr, t ~2 mm), a circular defect (d ~5 mm) was created with a drill press (Grizzly G7948). A “fitting temperature” (T_{fit}) was determined as the saline temperature that, after 1 min of submersion, consistently produced a scaffold that was malleable to the touch. A hot plate equipped with a digital temperature probe (Heidolph, MR HEI-TEC) was used to the warm saline in 1 °C intervals within a given scaffold’s onset to midpoint $T_{m,PCL}$ range (i.e. 50–56 °C for *linear*-PCL-based and 42–50 °C for *star*-PCL-based scaffolds). T_{fit} was determined to be ~55 °C (for *linear*-PCL-based scaffolds) and ~45 °C (for *star*-PCL-based scaffolds). Next, each scaffold specimen was subjected to the following protocol: (1) submerged into saline previously heated to the designated T_{fit} and maintained for 1 min; (2) removed and immediately press-fitted into a model defect (at RT); (3) maintained in the model defect for 2 min to fix the new temporary shape; (4) removed from the defect (pushing out by hand), allowed to sit for 2 min; (5) re-submerged into the saline bath at T_{fit} for 1 min to elicit shape recovery, removed, allowed to cool at RT for 2 min. At key points during this sequence, the scaffold diameter was measured using electronic calipers to quantify scaffold strain (ϵ). Steps 1–5 were repeated to determine shape fixity (R_f) and shape recovery (R_r) over a second cycle. From this process, the R_f and shape recovery R_r for the first ($N=1$) and second ($N=2$) cycles were calculated, according to Equations 4 and 5, respectively:

$$R_f(N) = \frac{\epsilon_u(N)}{\epsilon_m} \quad (4)$$

$$R_r(N) = \frac{\epsilon_m - \epsilon_p(N)}{\epsilon_m - \epsilon_p(N-1)} \quad (5)$$

where ε_m is the maximum strain following step 2, $\varepsilon_u(N)$ is the strain in the stress-free state following step 3, and ε_p is the final recovered strain following step 4. Strain values were determined via electronic caliper measurements.

Radial pressure during shape recovery.: Scaffold discs ($d \sim 6$ mm x $t \sim 2$ mm; $N = 5$) were subjected to radial mechanical testing (Instron 5965 equipped with a Blockwise RJA62 J-Crimp Radial Compression Station), to determine the radial pressure exerted during shape recovery at a scaffold's T_{fit} (*LPCL, L/L, L/S* at 55 °C and *SPCL, S/L, S/S* at 45 °C). This was intended to mimic shape recovery during self-fitting of the scaffold specimen into a $d \sim 5$ mm defect. Specimens were loaded into the bore set to an initial $d \sim 6.5$ mm at RT. The temperature was then increased to the designated T_{fit} and maintained for 3 min. Next, the bore diameter was reduced from 6.5 mm to 5 mm at a rate of 1 mm/min. Force was monitored throughout the procedure, and total radial force (TRF) was calculated and converted to radial pressure based on exact scaffold dimensions.⁵⁰

Solution viscosity and scaffold scale-up

Solution viscosity.: The complex viscosity [η^*] of each scaffold macromer precursor solutions ($N = 3$) was measured as a function of frequency (100 Hz to 0.1 Hz, Anton Parr MCR 301). Macromer solutions (0.15 g per mL of DCM) were comprised of *linear*-PCL-diol or *star*-PCL-tetrol (i.e. non-acrylated) and no photoinitiator solution to avoid cross-linking during the test. To determine the intrinsic viscosity, the η^* data was extrapolated to a theoretical zero shear rate (0 Hz).

Solution diffusion through salt template.: Select macromer solutions (*L/L* and *S/S*), containing dye, were used to assess differences in the rate of diffusion through a salt template. To aide inspection of diffusion, salt templates with a somewhat higher heights were prepared as above but with 15.0 g of sieved salt. Macromer solutions (~ 7.5 mL) were prepared with designated macromers (i.e. *linear*-PCL-DA and *linear*-PLLA or *star*-PCL-TA and *star*-PLLA), 15 vol% photoinitiator solution, and a few drops of food coloring. With two salt templates placed side-by-side, each macromer solution was gently poured over the template simultaneously and diffusion captured via video. The process was repeated in triplicate.

Scaled-up scaffold fabrication.: The *L/L* and *S/S* compositions were again selected to fabricate larger scaffolds due to their lowered solution viscosities. A 5 mm hole (diamond core drill bit, Marshalltown) was drilled into the bottom of a 100 mL beaker (I.D. = 43.6 mm) to aid in macromer solution diffusion. Each 100 mL beaker was filled with 50.0 g of salt and 7.5 wt% water was incorporated over 4 additions with mechanical mixing following each addition. A smaller beaker was used to manually push the wet salt down and the salt molds were vacuum dried (RT, 30 in. Hg., ON). Macromer solutions were prepared (~ 15 mL) according to that described above for fabrication of smaller scaffolds. Once mixed, macromer solution was poured on top of the fused salt mold and was allowed to sit for ~ 3 min to permit diffusion; aluminum foil covered the beaker to prevent premature UV curing and solvent evaporation. Following UV-cure (InetlliRay 400, 50% intensity) for 10 min, specimens were allowed to dry in a fume hood (48 hr) and were then soaked in a 1:1 DI

water:ethanol solution with daily solution changes. Dried scaffolds were then annealed and sliced into 2 mm specimens, as described above for the smaller scaffolds. Note, both types of scaffolds were maintained at their full diameter for size comparisons (ie. no biopsy punch was used). Photos were taken throughout the procedure and low magnification optical microscopy (Leica DM 6B; 5X) was performed on scaffold specimens to broadly examine pore morphology. The procedure was performed in triplicate and scaffolds were measured with electronic calipers to quantify dimensional changes. SEM (JEOL JCM-5000 Neoscope, accelerating voltage ~10 kV, Au-Pt coating ~4 nm) with energy dispersive X-ray spectroscopy (EDS, Oxford Instruments) elemental mapping was also performed to confirm complete porogen leaching from larger constructs.

Statistical analyses

All data was reported as the average \pm standard deviation. ANOVA tests were performed and if there was a statistical difference, t-tests were performed against the *LPCL* control. T-tests were also used to make direct comparisons between compositions of interest, which will be specified for each result discussed. For mechanical testing, interquartile range tests were performed and values that were determined as being outliers were removed from the data (final $N = 5$). For rheology data, linear regression was used to extrapolate complex viscosity to zero shear. Regression analyses were only performed up to 1 Hz to achieve $R^2 > 0.5$ and zero shear viscosities were reported as averages \pm the standard error.

Results and discussion

Macromer synthesis

Linear- and *star*-PLLA ($M_n \sim 15$ kg/mol) (Figure S1) as well as *linear*-PCL-diol and *star*-PCL-tetrol ($M_n \sim 10$ kg/mol) (Figure S2) were characterized. Star macromer M_n was selected to match previously studied linear macromers in order to rule out M_n as a variable. As described above, ^1H NMR end group analysis was used to determine M_n and confirm architecture (i.e. terminal group protons were approximately doubled for star precursors). DSC was used to determine thermal transitions and % crystallinity, with differences in thermal properties used to further validate precursor architecture. The T_g and T_m values as well as % crystallinity varied for the *linear*-PLLA ($T_g \sim 45$ °C, $T_m \sim 155$ °C, ~50%) versus the *star*-PLLA ($T_g \sim 49$ °C, $T_m \sim 152$ °C, ~15%). Likewise, differences were observed for the T_g , T_m , and % crystallinity values of the *linear*-PCL diol ($T_g \sim -65$ °C, $T_m \sim 53$ °C, ~48%) and the *star*-PCL tetrol ($T_g \sim -63$ °C, $T_m \sim 50$ °C, ~45%). Subsequently, the *linear*-PCL diol and *star*-PCL tetrol were successfully acrylated (>85%) to yield *linear*-PCL-DA and *star*-PCL-TA, respectively (Figure S3).

Scaffold fabrication

Fabricated scaffolds were characterized in various ways to ensure effective cross-linking (sol content), to confirm the targeted PCL/PLLA wt% ratio of 75:25 (TGA), and to quantify pore size and % porosity (SEM and density calculations, respectively). Sol content values for 100% PCL controls [*LPCL* and *SPCL*] was just 2–4 %, further indicating successful cross-linking (i.e. > 95%) (Figure S4). All semi-IPN scaffolds displayed sol content values < 29%, similar to the controls when the thermoplastic PLLA (incorporated at 25 wt%) was

considered. Additionally, the TGA thermograms of semi-IPNs all showed ~25 wt% mass loss from 250–350 °C that corresponded to the 25 wt% PLLA contained (Figure S5). Thus, the PLLA did not diminish *linear*-PCL-DA or *star*-PCL-TA cross-linking and the targeted 75/25 wt% ratio of PCL/PLLA was maintained. Finally, SEM imaging and analysis confirmed the targeted pore interconnectivity and ~220 µm average pore size (Figure S6a), within the range associated with osteogenesis.⁵¹ Porosity calculations revealed that all scaffolds were similarly ~60% (Figure S6b).

Scaffold thermal properties

PCL T_m .—The midpoint melting temperature of PCL ($T_{m,PCL}$) represents the temperature to which the scaffold must be heated to confer *maximum* shape recovery, key to self-fitting into the bone defect. The T_m values were quantified for all scaffold compositions (Figure 2a, Table S1). Notably, the midpoint $T_{m,PCL}$ values were significantly reduced (~6 °C) for *star*-PCL-based versus *linear*-PCL-based scaffolds. The *LPCL* scaffold had a $T_{m,PCL}$ ~56 °C (midpoint) that was maintained following incorporation of *linear*- or *star*-PLLA to form *L/L* and *L/S* semi-IPN scaffolds, respectively. In contrast, for the *SPCL* scaffold, the $T_{m,PCL}$ (midpoint) was significantly reduced to ~50 °C. These values were maintained with the incorporation of *linear*- or *star*-PLLA to form *S/L* and *S/S* semi-IPNs, respectively. As is discussed later, *star*-PCL-based scaffolds begin to soften and undergo self-fitting in model defects at temperatures below $T_{m,PCL}$ ~50 °C (midpoint), due to the fact that the onset melting temperature of PCL is just ~42 °C (Figure 2b, Table S1). This presented a unique way to afford a tunable $T_{m,PCL}$ in a chemically cross-linked PCL scaffold. In contrast, we previously tuned linear PCL M_n (~10 kg/mol and ~5 kg/mol), but this did not yield appreciable differences in scaffold $T_{m,PCL}$ (56.2 ± 0.4 and 54.4 ± 0.6 °C, respectively).¹⁶ In this way, *star*-PCL-based compositions are expected to improve tissue safety during self-fitting into bone defects.

PCL crystallinity.—PCL crystalline lamellae are the origin of shape memory behavior and thus self-fitting behavior and further have a significant impact on degradation and mechanical properties. Thus, scaffold PCL % crystallinity was quantified from DSC (Figure S7a, Table S1). For *LPCL*, PCL % crystallinity was ~42%. When corrected for weight % in semi-IPN compositions (PCL/PLLA, 75/25 wt%), PCL % crystallinity was maintained for *linear*-PCL-based semi-IPNs (i.e. *L/L* and *L/S*). In the case of *SPCL*, PCL crystallinity was significantly reduced to ~30%. As described later, the PCL % crystallinity of all scaffolds was sufficient to retain similarly shape recovery and shape fixity. However, the addition of *linear*- or *star*-PLLA to form *S/L* and *S/S* semi-IPNs resulted in increased PCL crystallinity of ~34% and ~39% (with *S/S* similar to the *LPCL* control), respectively.

PLLA crystallinity.—PLLA crystallinity will impact scaffold degradation and mechanical properties. The previously reported *L/L* semi-IPN scaffold exhibited PLLA crystallinity (~38%) and $T_{m,PLLA}$ (midpoint) (164 °C) (Table S1, Figure S7b). When *star*-PLLA was incorporated into the *linear*-PCL-DA network, the resulting *S/L* semi-IPN scaffold exhibited significantly decreased PLLA crystallinity (~20%, ~158 °C). For *star*-PCL-based semi-IPNs, the PLLA crystallinity was somewhat intermediate: *S/L* (~23%, ~160 °C) and *S/S* (~25%, ~157 °C), but was not statistically significant compared to the *L/L*. Thus, versus the *L/L*

semi-IPN scaffolds, the *S/L*, *S/L*, and *S/S* had somewhat diminished PLLA crystallinity and is considered in analysis of degradation and mechanical properties.

Degradation behavior

Previously, we reported that the *L/L* semi-IPN scaffold degraded significantly faster than the *LPCL* control.^{16, 22, 23} Further acceleration of degradation is anticipated to favorably allow neotissue formation as well as osteogenesis.^{17, 19–21} This present study revealed that the *L/S* semi-IPN degraded faster than the *L/L* semi-IPN (Figure 3a). In the case of *star*-PCL-based compositions, the *SPCL* scaffold degraded slowly, similar to *LPCL* (Figure 3b). However, the *S/L* and *S/S* semi-IPNs degraded faster and generally similar to each other. By examining mass loss at the 72 hr timepoint (Figure 3c) as well as images of specimens at increasing time points (Figure 3d), it is clear that *S/L* and *S/S* exhibited the most rapid rate of mass loss, even faster than *L/S*. Notably, mass loss at earlier timepoints (48 hr) was greater for *S/S* versus *S/L*. While reduced levels of PCL and/or PLLA % crystallinity of semi-IPNs (Table S1, Figure S7) would be predicted to increase their rate of degradation, these properties were not always correlative. For instance, the *L/S* and *S/S* showed similar PCL % crystallinity (~40%), and the *L/S* showed a lower PLLA % crystallinity (~20% compared to 25%), but the *S/S* degraded significantly faster than the *L/S*. Thus, PCL/PLLA phase separation was considered, as this has been known to contribute to accelerated degradation of blends^{25, 26} and semi-IPNs.^{16, 23, 24} SEM of analogous solid films demonstrated distinct morphologies for each composition (Figure S8). Both 100% PCL controls [*LPCL* and *SPCL*] showed a uniform morphology as expected based on their chemical homogeneity. The *L/L* (i.e. slowest degrading semi-IPN) also showed minimal signs of phase separation. However, all other semi-IPNs [*L/S*, *S/L* and *S/S*] showed greater evidence of coalescence, indicative of greater phase separation or immiscibility.^{24, 52, 53} Further, these new semi-IPN scaffolds demonstrate the potential to both accelerate and tune scaffold degradation rates based on phase separation. The current results were limited to base-catalyzed conditions, known to impact polyester degradation kinetics.⁵⁴ Thus, future studies wherein scaffold degradation is assessed *in vitro* under physiological conditions as well as *in vivo* would be informative. PCL has been known to degrade *in vivo* over the course of ~2 years,^{55, 56} but these faster degrading scaffolds are expected to more closely mimic the timescale of CMF bone regeneration (3 to 6 months).²¹ As rates of regeneration can vary due to patient age and other factors,⁵⁷ the tunability of these scaffolds' degradation rates may be advantageous.

Mechanical, shape memory, and radial expansion pressure properties

Mechanical properties.—Mechanically robust SMP scaffolds are expected to afford superior outcomes in the treatment of bone defects. Static compressive testing was performed to assess the compressive mechanical properties of the SMP scaffolds. For *linear*-PCL-based compositions, versus the *LPCL* control (~9.65 MPa), the modulus (E) was significantly increased for both the *L/L* (~23.8 MPa) and *L/S* (~17.4 MPa) semi-IPNs (Figure 4a, Table S2). In terms of *star*-PCL-based compositions, for the *SPCL* control (~3.57 MPa), E was significantly lower than the *LPCL*. This was attributed to the former's reduced PCL % crystallinity, in spite of having a higher relative cross-link density. However, versus

the *SPCL*, E was increased for the *S/L* (~11.9 MPa) and *S/S* (~11.3 MPa) semi-IPNs, similar to the *LPCL* control. All semi-IPNs exhibited higher E values versus the 100% PCL controls, but the E values of *L/L* and *L/S* were higher than that of *S/L* and *S/S*. Similar trends generally emerged for compressive strength (CS) (Figure 4b) as well as for toughness (Figure 4c). No scaffold fractured during the test (i.e. withstood 85% strain), indicative of their non-brittle behavior that is desirable in the intended application of CMF bone defect treatment. Moreover, all scaffold compositions demonstrated robust mechanical properties for handling and press-fitting. Of all compositions, the *L/S* semi-IPN exhibited the greatest CS and toughness, while the *S/L* semi-IPN exhibited enhanced CS and toughness versus the *SPCL* control. Thus, a *star*-architecture affords certain semi-IPNs (*L/S* and *S/L*) with particularly notable mechanical properties.

Self-fitting properties.—Scaffold specimens (d ~6 mm x t ~2 mm) were press-fitted into a plastic model defect (d ~5 mm x t ~2 mm). This defect represented a rat bilateral calvarial defect model of the same dimensions, typically used as an entry-level model for bone defect healing studies.^{49, 58} A slighter larger scaffold diameter was selected to promote contact along the defect perimeter. Herein, scaffolds were fitted in the same fashion envisioned a clinical setting (Figure 5a, b). A T_{fit} was the minimum saline bath temperature that in just 1 minute produced a softened, malleable scaffold: ~55 °C for *linear*-PCL-based and ~45 °C for *star*-PCL-based scaffolds. A sequence of steps was used to assess self-fitting and ultimately quantify R_f and R_r (Figure 5c, Figure S9). Following submersion in saline at T_{fit} for 1 minute [step 1], all scaffolds were successfully press-fitted into defects (i.e. expanded via shape recovery to fill the defect) [step 2]. After just 2 minutes within the defect, scaffolds returned to their relatively rigid state (i.e. underwent shape fixation in new shape within the defect) [step 3]. Next, scaffolds were removed from the defect and allowed to sit for 2 min (to determine shape fixity) [step 4] and reheated at T_{fit} in saline for 1 minute (to determine shape recovery) [step 5]. For both cycles, these values were consistently at or near 100% for all scaffolds. These results further validate that the semi-IPN design, based on any combination of *linear*-PCL-DA or *star*-PCL-TA and both *linear*-PLLA or *star*-PLLA, does not compromise shape memory behavior. However, as osteonecrosis begins to occur with exposure to temperatures > 50 °C,⁵⁹ the lower T_{fit} of *star*-PCL-based scaffolds (i.e. *SPCL*, *S/L*, and *S/S*) is more “tissue-safe”. Furthermore, the observed T_{fit} of 45 °C is considered ideal for self-fitting CMF bone scaffolds, as it is sufficiently above T_{body} and so exists in a rigid state within the defect to support healing.

Radial pressure.—For the first time, we report the radial pressures exerted by the SMP scaffolds during self-fitting at their T_{fit} to quantify the force exerted by the scaffold against the defect edges, driven by shape recovery (Figure 5d). The pressure was monitored while a scaffold (d ~ 6mm x t ~2 mm), initially loaded into a bore (d ~6.5 mm) at RT, was heated to its T_{fit} and the bore diameter then reduced to that of a calvarial defect (d ~5 mm). Versus the *LPCL* control (~57 kPa), radial pressure significantly increased for the *L/L* (~195 kPa) and *L/S* (~162 kPa) semi-IPNs, attributed to the rigid PLLA. The radial pressure of the *SPCL* (~127 kPa) was also much higher than the *LPCL*, which may be attributed to its higher crosslink density. A further substantial increase in radial pressure was noted for the *S/L* (~239 kPa) and *S/S* (~188 kPa) versus the *SPCL*, again stemming from the rigid PLLA.

Thus, the substantial gains in radial pressure (versus the *LPCL* control) observed for the *SPCL* and all semi-IPNs affords improved scaffold expansion toward defect edges during self-fitting, which is anticipated to promote osseointegration and overall implant stability *in vivo*.

Solution viscosity and scaffold scale-up—In the aforementioned analyses, SMP scaffolds were prepared with a diameter of ~6 mm (biopsy punch of a scaffold with $d \sim 12$ mm); this size is appropriate for bilateral rat calvarial defect studies. However, larger scaffolds are necessary for critically-sized defects in animal models (up to $d \sim 22$ mm)⁶⁰ and eventually for human patients. While centrifugation to drive diffusion is permissible for small scaffolds that are prepared in scintillation vials, this is not the case for larger scaffolds. Because *star*-polymers are known to have a lowered solution viscosity,^{43, 44} we expected that SMP scaffolds prepared with such would more readily permit the preparation of larger specimens. First, the complex viscosity [η^*] of scaffold precursor solutions were determined over a frequency sweep (Figure 6a) and the intrinsic viscosity calculated by extrapolation to a zero-shear rate (Figure 6b). Both 100% PCL controls (*LPCL* and *SPCL*), exhibited a relatively high intrinsic viscosity (~9 kPa*s). For semi-IPN macromer solutions containing *linear*-PCL, intrinsic viscosity was reduced with *star*-PLLA (*L/S*; ~1 kPa*s) versus with *linear*-PLLA (*L/L*; ~6 kPa*s). Semi-IPN macromer solutions based on *star*-PCL were likewise reduced, particularly with *star*-PLLA (*S/S*; ~1 kPa*s) versus with *linear*-PLLA (*S/L*; ~6 kPa*s). Because of their relatively high and low intrinsic viscosities, respectively, *L/L* and *S/S* semi-IPN macromer solutions were selected to prepare larger scaffold specimens. First, using fused salt templates prepared in scintillation vials, diffusion of the precursor solutions containing food coloring was monitored (Figure 6c, Video S1). Owing to its lower intrinsic viscosity, the *S/S* solution diffused more quickly to the bottom of the template (~90 s) versus the *L/L* solution (>120 s). Next, *L/L* and *S/S* were prepared as actual scaled-up, “larger” scaffolds, using 100 mL beakers (50 g salt) in place of the 20 mL vials (10 g salt). Analogous “regular” scaffolds were prepared in the 20 mL vials (10.0 g salt), but the diameter was not reduced from ~12 mm using a biopsy punch. Thus, the “larger” scaffolds had a diameter and volume that was 2X and 5X, respectively, that of the “regular” scaffolds (Figure S10a,b). For the “large” *S/S* scaffolds, a total of four 2 mm thick specimens (i.e. slices) could be harvested versus just three 2 mm thick slices for the “larger” *L/L* scaffolds (Figure 7). This stemmed from a lack of diffusion, wherein the *L/L* macromer solution did not reach the bottom of the mold, rendering the bottom portion deficient. While density did not change according to gravimetric analysis (Figure S10c), low magnification optical microscopy revealed that *S/S* demonstrated superior uniformity of pores throughout versus the *L/L*. Full porogen leaching has been previously noted as a limitation in SCPL fabrication;⁶¹ however, herein the NaCl porogen used in fabrication was shown to be fully removed even from “larger” scaffolds, likely owing to the use of a fused salt template resulting in interconnected pores. This was validated via SEM and EDS mapping to show that the scaffolds did not contain any appreciable amount of Na or Cl (Figure S11). Lastly, as a further indicator of their utility as a surgical product to treat bone defects, the *S/S* scaffold was able to be trimmed with a scissor and also sutured (Figure 8a).

Conclusions

Towards improving the utility of “self-fitting” SMP scaffolds, semi-IPN compositions were prepared with *star*-polymer architectures. Originally prepared from *linear*-PCL-DA and *linear*-PLLA (75/25 wt%), the *L/L* semi-IPN exhibited improved rigidity and accelerated degradation versus *linear*-PCL-DA (*LPCL*). In this work, the semi-IPN based on *star*-PCL-TA and *star*-PLLA (*S/S*) (75/25 wt%) exhibited distinct advantages and fulfilled key criteria as a surgical product to treat CMF bone defects (Figure 8b). The pore size (~200 μm) and pore interconnectivity, to promote osteogenesis and to favorably allow neotissue infiltration, was maintained using the SCPL fabrication protocol. While this study was limited to *in vitro* material characterization, the *LPCL* control scaffold had been previously shown to support osteogenesis, which was improved with the addition of cell adhesion motifs and bioactive coatings.^{12, 13} The new scaffold compositions are expected to yield favorable and potentially improved results in such cell culture studies. Importantly, self-fitting of the *S/S* semi-IPN scaffold could be performed at a more tissue-safe, lower T_{fit} (~45 °C) versus for the *L/L* semi-IPN scaffold (~55 °C). The *S/S* semi-IPN exhibited similar rigidity versus the original *LPCL*, although it was somewhat less rigid and strong versus the *L/L* semi-IPN. Despite this, radial pressure during shape recovery at T_{fit} for the *S/S* semi-IPN was shown to be significantly improved versus for the *LPCL* and was similar to that of the *L/L* semi-IPN. This ability to expand with greater force toward the defect edges during self-fitting is expected to improve scaffold osseointegration and implant prior to healing. Additionally, the *S/S* semi-IPN exhibited even faster degradation versus the *L/L* semi-IPN, and so is expected to better promote neotissue infiltration. Finally, the reduced intrinsic viscosity of *S/S* semi-IPN precursor solution improved its diffusion through the salt template (in the absence of centrifugation), permitting larger scaffolds to be prepared. Thus, *star*-polymer architectures were successfully leveraged to create “self-fitting” SMP scaffolds with properties better suited for treatment of CMF bone defects.

Supplementary Material

Refer to Web version on PubMed Central for supplementary material.

Acknowledgements

This work was supported by NIH NIDCR 1R01DE025886-01A1. The use of the Texas A&M Microscopy and Imaging Center is acknowledged. The FE-SEM acquisition was supported in part by the National Science Foundation under Grant No. DBI-0116835.

References

1. Parithimarkalaignan S and Padmanabhan TV, J Indian Prosthodont Soc, 2013, 13, 2–6. [PubMed: 24431699]
2. Doi K, Kubo T, Makihara Y, Oue H, Morita K, Oki Y, Kajihara S and Tsuga K, J Appl Oral Sci, 2016, 24, 325–331. [PubMed: 27556202]
3. Neovius E and Engstrand T, J Plast Reconstr Aesthet Surg, 2010, 63, 1615–1623. [PubMed: 19577527]
4. Phillips JH and Rahn BA, Plast Reconstr Surg, 1990, 85, 891–897. [PubMed: 1693441]
5. Moghadam HG, Implant Dent, 2009, 18.

6. Low KL, Tan SH, Zein SHS, Roether JA, Mouriño V and Boccaccini AR, *J Biomed Mater Res Part B Appl Biomater*, 2010, 94B, 273–286.
7. Shah AM, Jung H and Skirboll S, *Neurosurg Focus*, 2014, 36, E19. [PubMed: 24684331]
8. Lennon AB and Prendergast PJ, *J Biomech*, 2002, 35, 311–321. [PubMed: 11858806]
9. Lobb DC, DeGeorge BR and Chhabra AB, *J Hand Surg*, 2019, 44, 497–505.e492.
10. Orr JF, Dunne NJ and Quinn JC, *Biomaterials*, 2003, 24, 2933–2940. [PubMed: 12742733]
11. Haleem A and Javaid M, *Clin Epidemiol Glob Health*, 2019, 7, 571–577.
12. Zhang D, George OJ, Petersen KM, Jimenez-Vergara AC, Hahn MS and Grunlan MA, *Acta Biomater*, 2014, 10, 4597–4605. [PubMed: 25063999]
13. Erndt-Marino JD, Munoz-Pinto DJ, Samavedi S, Jimenez-Vergara AC, Diaz-Rodriguez P, Woodard L, Zhang D, Grunlan MA and Hahn MS, *ACS Biomater Sci Eng*, 2015, 1, 1220–1230. [PubMed: 33304994]
14. Zhang D, Petersen KM and Grunlan MA, *ACS Appl Mater Interfaces*, 2013, 5, 186–191. [PubMed: 23227875]
15. Nail LN, Zhang D, Reinhard JL and Grunlan MA, *JoVE*, 2015, DOI: doi:10.3791/52981., e52981. [PubMed: 26556112]
16. Woodard LN, Kmetz KT, Roth AA, Page VM and Grunlan MA, *Biomacromolecules*, 2017, 18, 4075–4083. [PubMed: 29037044]
17. Park S-H, Gil ES, Kim HJ, Lee K and Kaplan DL, *Biomaterials*, 2010, 31, 6162–6172. [PubMed: 20546890]
18. Hollister SJ, *Nat Mater*, 2005, 4, 518–524. [PubMed: 16003400]
19. Langer R and Tirrell DA, *Nature*, 2004, 428, 487–492. [PubMed: 15057821]
20. Dhandayuthapani B, Yoshida Y, Maekawa T and Kumar DS, *Int J Polym Sci*, 2011, 2011, 290602.
21. Bose S, Roy M and Bandyopadhyay A, *Trends Biotechnol*, 2012, 30, 546–554. [PubMed: 22939815]
22. Woodard LN, Page VM, Kmetz KT and Grunlan MA, *Macromol Rapid Commun*, 2016, 37, 1972–1977. [PubMed: 27774684]
23. Woodard LN and Grunlan MA, *ACS Biomater Sci Eng*, 2019, 5, 498–508. [PubMed: 31633012]
24. Pfau MR, McKinzey KG, Roth AA and Grunlan MA, *Biomacromolecules*, 2020, 21, 2493–2501.
25. Tsuji H and Ikada Y, *J Appl Polym Sci*, 1998, 67, 405–415.
26. Arias V, Höglund A, Odelius K and Albertsson A-C, *Biomacromolecules*, 2014, 15, 391–402. [PubMed: 24279455]
27. Ostafinska A, Fortelny I, Nevoralova M, Hodan J, Kredatusova J and Slouf M, *RSC Adv*, 2015, 5, 98971–98982.
28. Urquijo J, Guerrica-Echevarría G and Eguiazabal JI, *J Appl Polym Sci*, 2015, 132, 42641.
29. Wu W, Wang W and Li J, *Prog Polym Sci*, 2015, 46, 55–85.
30. Jahandideh A and Muthukumarappan K, *Eur Polym J*, 2017, 87, 360–379.
31. Michalski A, Brzezinski M, Lapienis G and Biela T, *Prog Polym Sci*, 2019, 89, 159–212.
32. Li Y and Kissel T, *Polymer*, 1998, 39, 4421–4427.
33. Kim ES, Kim BC and Kim SH, *J Polym Sci, Part B: Polym Phys*, 2004, 42, 939–946.
34. Ghoorchian A and Holland NB, *Biomacromolecules*, 2011, 12, 4022–4029. [PubMed: 21972921]
35. Breitenbach A, Li YX and Kissel T, *Journal of controlled release : official journal of the Controlled Release Society*, 2000, 64, 167–178. [PubMed: 10640655]
36. Burke J, Donno R, d'Arcy R, Cartmell S and Tirelli N, *Biomacromolecules*, 2017, 18, 728–739. [PubMed: 27930884]
37. Atthoff B, Trollsås M, Claesson H and Hedrick JL, *Macromol Chem Phys*, 1999, 200, 1333–1339.
38. Huang C-F, Kuo S-W, Lin H-C, Chen J-K, Chen Y-K, Xu H and Chang F-C, *Polymer*, 2004, 45, 5913–5921.
39. Theodorakis PE, Avgeropoulos A, Freire JJ, Kosmas M and Vlahos C, *Macromolecules*, 2006, 39, 4235–4239.
40. Singh C and Balazs AC, *Polym Int*, 2000, 49, 469–471.

41. Bian X, Zhang B, Sun B, Sun Z, Xiang S, Li G and Chen X, *Polym Eng Sci*, 2016, 56, 1125–1137.
42. Mauck SC, Wang S, Ding W, Rohde BJ, Fortune CK, Yang G, Ahn S-K and Robertson ML, *Macromolecules*, 2016, 49, 1605–1615.
43. Lu Y, An L and Wang Z-G, *Macromolecules*, 2013, 46, 5731–5740.
44. Douglas JF, Roovers J and Freed KF, *Macromolecules*, 1990, 23, 4168–4180.
45. Kaihara S, Matsumura S, Mikos AG and Fisher JP, *Nat Protoc*, 2007, 2, 2767–2771. [PubMed: 18007612]
46. Pitt CG, Chasalow FI, Hibionada YM, Klimas DM and Schindler A, *J Appl Polym Sci*, 1981, 26, 3779–3787.
47. Fukushima K, *Polym Degrad Stabil*, 2011, v. 96, pp. 2120–2129-2011 v.2196 no.2112.v.
48. Zong C, Xue D, Yuan W, Wang W, Shen D, Tong X, Shi D, Liu L, Zheng Q, Gao C and Wang J, *Eur Cell Mater*, 2010, 20, 109–120. [PubMed: 21249628]
49. Shirakata Y, Nakamura T, Shinohara Y, Taniyama K, Sakoda K, Yoshimoto T and Noguchi K, *J Mater Sci Mater Med*, 2014, 25, 899–908. [PubMed: 24363067]
50. Wierzbicki MA, Bryant J, Miller MW, Keller B and Maitland DJ, *J Mech Behav Biomed Mater*, 2016, 59, 156–167. [PubMed: 26766327]
51. Abbasi N, Hamlet S, Love RM and Nguyen N-T, *J Sci Adv Mater Med*, 2020, 5, 1–9.
52. Lyu S-P, Bates FS and Macosko CW, *AIChE Journal*, 2000, 46, 229–238.
53. Van Hemelrijck E, Van Puyvelde P, Velankar S, Macosko CW and Moldenaers P, *J Rheol*, 2003, 48, 143–158.
54. Burkersroda F. v., Schedl L and Göpferich A, *Biomaterials*, 2002, 23, 4221–4231. [PubMed: 12194525]
55. Sun H, Mei L, Song C, Cui X and Wang P, *Biomaterials*, 2006, 27, 1735–1740. [PubMed: 16198413]
56. Doppalapudi S, Jain A, Khan W and Domb AJ, *Polym Adv Technol*, 2014, 25, 427–435.
57. Velasco MA, Narváez-Tovar CA and Garzón-Alvarado DA, *Biomed Res Int*, 2015, 2015, 729076–729076. [PubMed: 25883972]
58. Bosch C, Melsen B and Vargervik K, *J Craniofac Surg*, 1998, 9, 310–316. [PubMed: 9780924]
59. Timon C and Keady C, *Cureus*, 2019, 11, e5226–e5226. [PubMed: 31565628]
60. Szpalski C, Barr J, Wetterau M, Saadeh PB and Warren SM, *Neurosurg Focus*, 2010, 29, E8.
61. Janik H and Marzec M, *Mater Sci Eng C Mater Biol Appl*, 2015, 48, 586–591. [PubMed: 25579961]

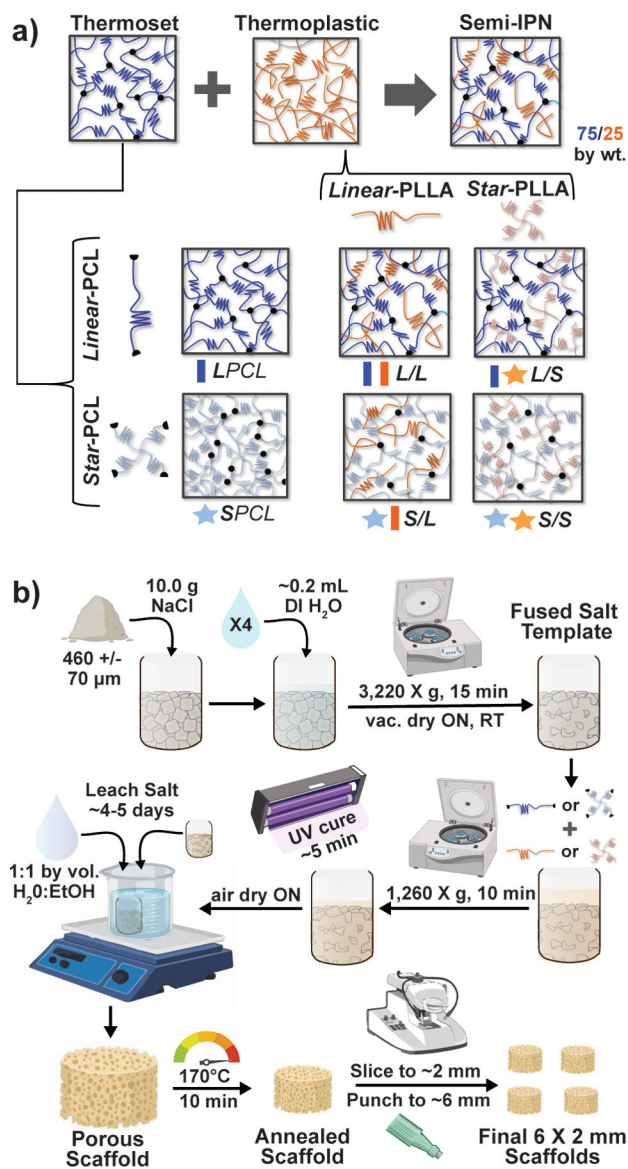


Figure 1. (a) four semi-ipn smp scaffolds were prepared with combinations of linear-pcl-da or star-pcl-ta and linear-plla or star-plla (75/25 pcl/plla). two 100% pcl controls were also prepared from linear-pcl-da or star-pcl-ta. (b) all smp scaffolds were prepared via solvent-casting/particulate leaching (scpl) whereby a designated solvent-based macromer solution was sequentially cast over a fused salt template, uv-cured, and the template extracted to yield highly interconnected pores.

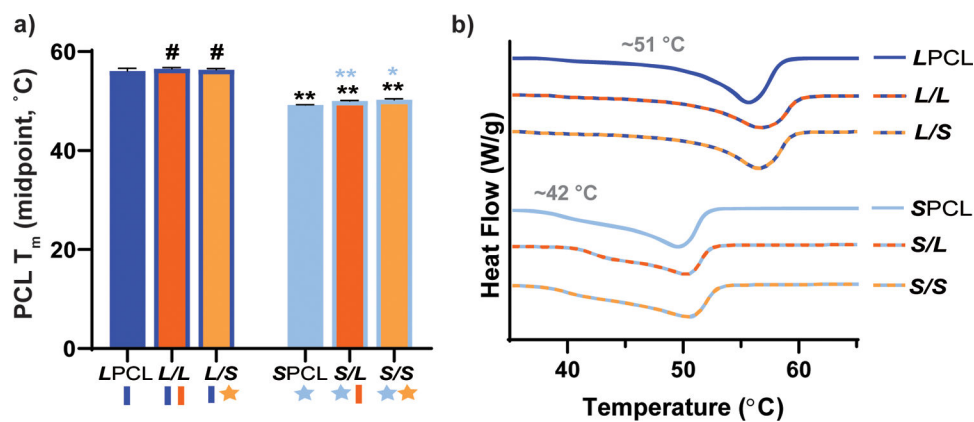


Figure 2.

(a) midpoint t_m of pcl of scaffolds; * $p < 0.05$, ** $p < 0.01$, # $p > 0.05$. note: the black color-coded statistics are comparisons to lpcl and blue color-coded statistics are comparisons to spcl. (b) representative thermogram for each scaffold composition.

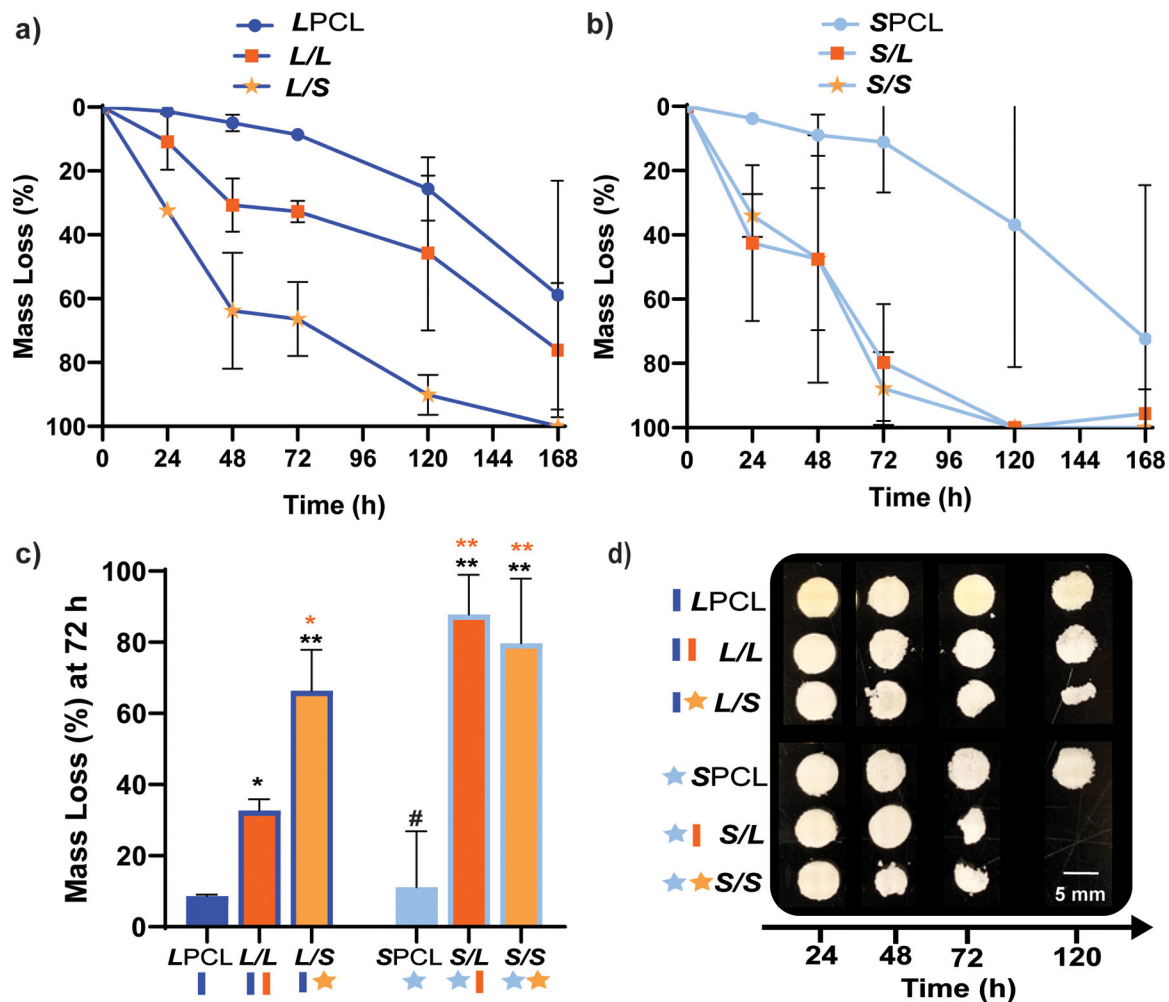


Figure 3. gravimetric mass loss over time for base-catalyzed degradation studies (0.2 m naoh, 37 c, 60 rpm) for (a) linear-pcl-based and (b) star-pcl-based scaffolds. (c) mass loss at 72 hr was compared for all scaffold compositions; * $p < 0.05$, ** $p < 0.01$, # $p > 0.05$. note: the black color-coded statistics were compared to lpcl control while orange color-coded statistics were compared to the l/l composition. (d) representative photos of specimens at different timepoints during degradation study.

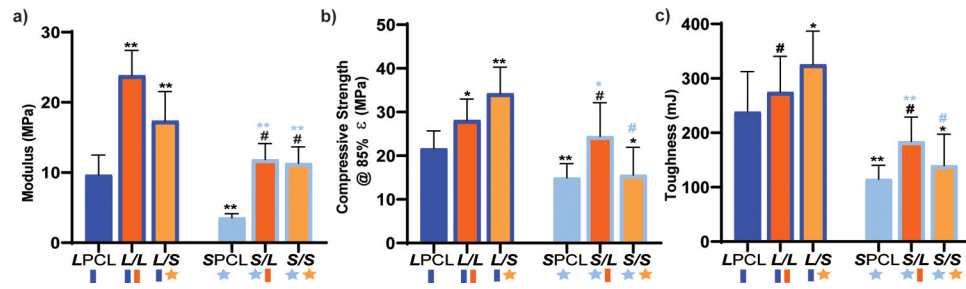


Figure 4.

compressive mechanical properties were compared including (a) e, (b) cs, and (c) toughness; * $p < 0.05$, ** $p < 0.01$, # $p > 0.05$. note: the black color-coded statistics are compared to the lpcl and light blue color-coded statistics are compared to spcl.

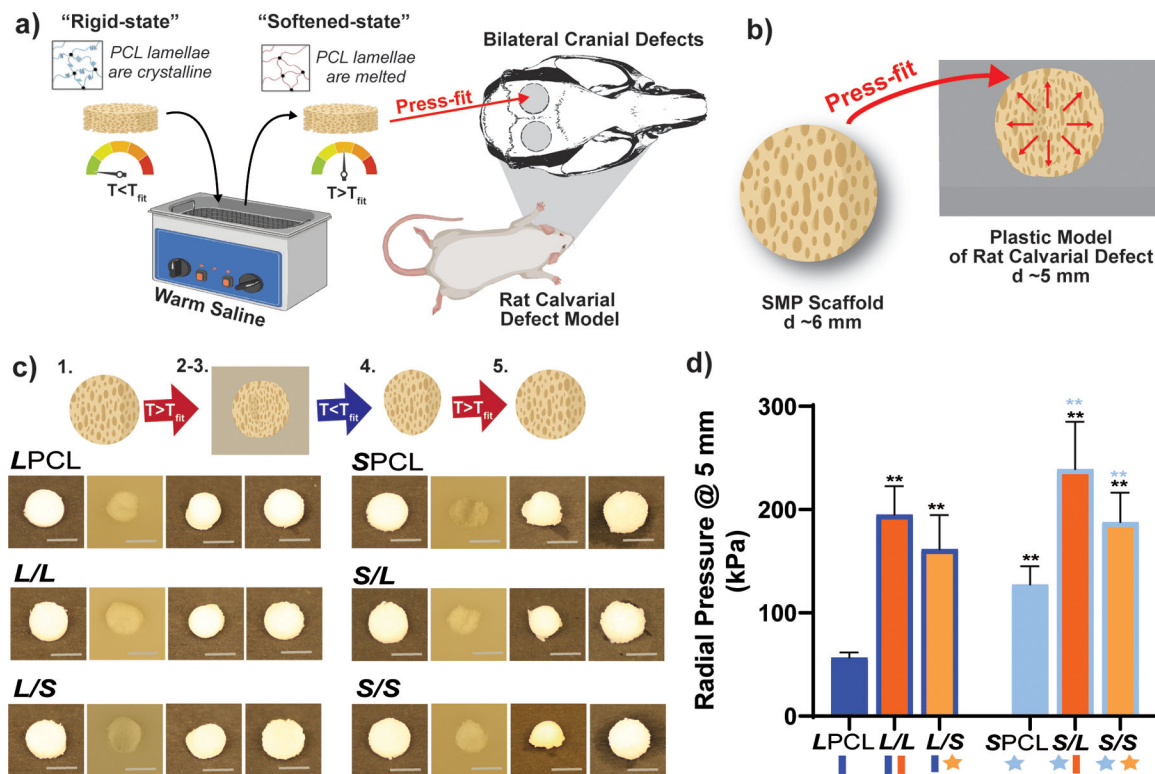


Figure 5.

(a) shape memory testing was performed to mimic a bilateral rat calvarial defect model *in vivo* study. (b) scaffolds were designed to be slightly larger than the cranial defect, so the warm scaffold will exert a force on the defect edges, as shown in the schematic. (c) all compositions were able to be press-fitted into a plastic model defect and demonstrated excellent shape fixity/recovery. protocol: following submersion in saline at T_{fit} for 1 minute [step 1], all scaffolds were successfully press-fitted into defects (i.e. expanded via shape recovery to fill the defect) [step 2]. after just 2 minutes within the defect, scaffolds returned to their relatively rigid state (i.e. underwent shape fixation in new shape within the defect) [step 3]. next, scaffolds were removed from the defect and allowed to sit for 2 min (to determine shape fixity) [step 4] and reheated at T_{fit} in saline for 1 minute (to determine shape recovery) [step 5]. (d) radial expansion pressure tested at T_{fit} ; * $p < 0.05$, ** $p < 0.01$. note: black color-coded statistics are compared to lpcl and “blue color-coded” statistics are compared to spcl.

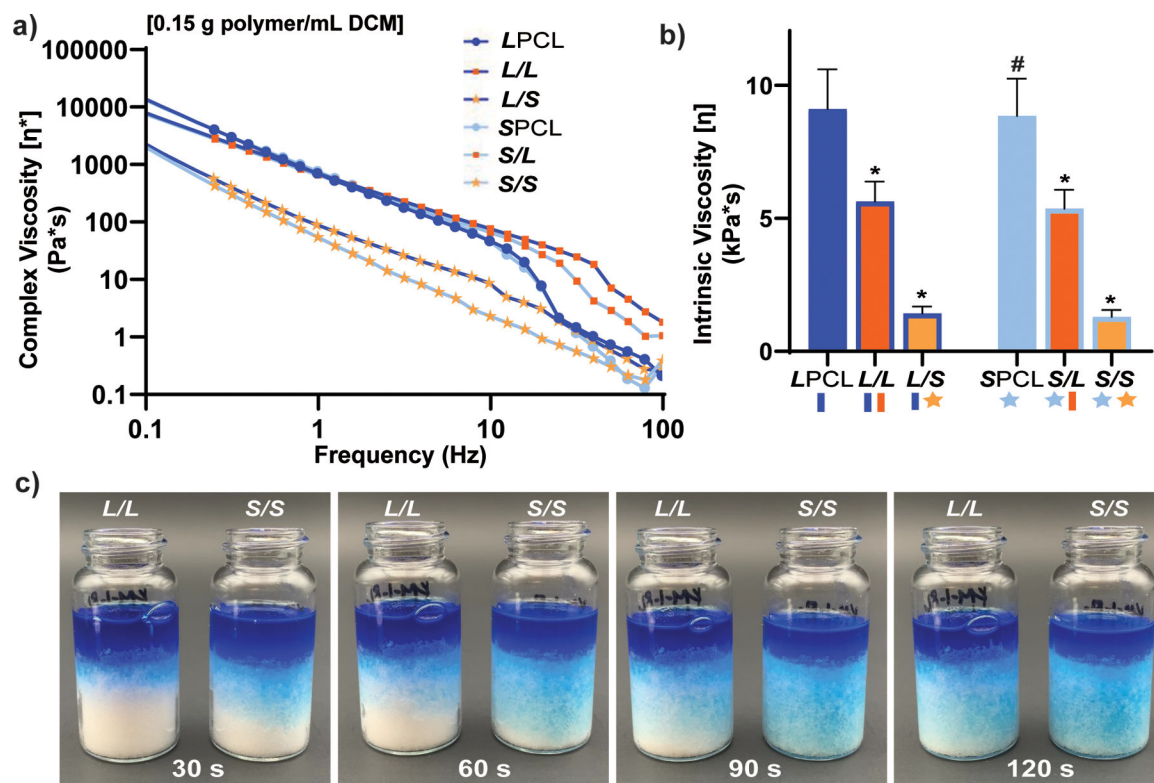


Figure 6. for scaffold precursor solutions: (a) complex viscosity [η^*] versus frequency, (b) intrinsic viscosity (* $p < 0.05$, ** $p < 0.01$ compared to lpcl). (c) l/l and s/s semi-ipn macromer solution diffusion through a template using 15.0 g salt in a scintillation vial.

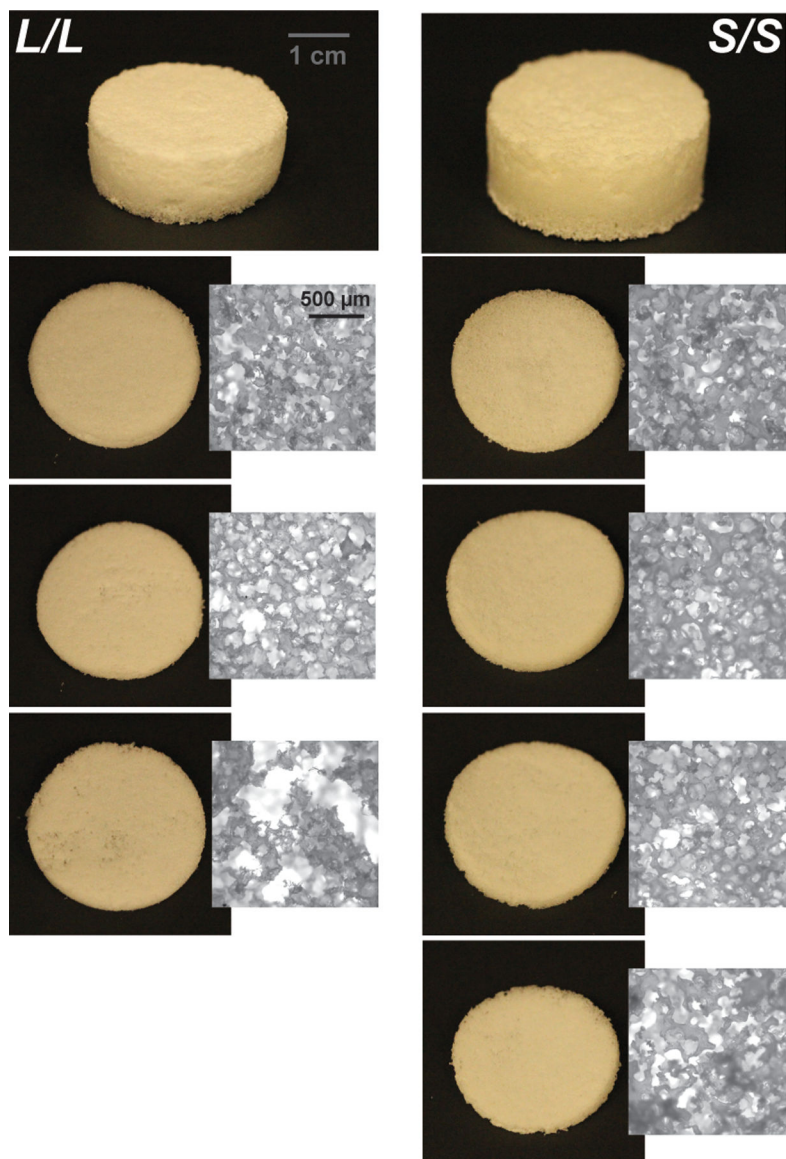


Figure 7. photos and optical microscopy (5x) of scaled-up, “large” l/l and s/s scaffolds (d ~24 mm) demonstrating superior macromer diffusion, and more uniform pores, for the s/s composition.

